Virtual prototyping of vision-based tactile sensors design for robotic-assisted precision machining

Islam Mohamed Zaid [a,b], Hussain Sajwani [b], Mohamad Halwani [a,b], Hany Hassanin [c,*],
Abdulla Ayyad [a,b], Laith AbuAssi [a,b], Fahad Almaskari [b], Yarjan Abdul Samad [b,d],
Abdulqader Abusafieh [a,e], Yahya Zweiri [a,b]

[a] Advanced Research and Innovation Center, Khalifa University, 127788, Abu Dhabi, United Arab Emirates
[b] Department of Aerospace Engineering, Khalifa University, 127788, Abu Dhabi, United Arab Emirates
[c] School of Engineering, Technology, and Design, Canterbury Christ Church University, Canterbury CT1 1QU, UK
[d] Cambridge Graphene Center, University of Cambridge, Cambridge CB3 0FA, UK
[e] Research and Development, Strata Manufacturing, PJSC, Al Ain 86519, United Arab Emirates

ARTICLE INFO

ABSTRACT

Vision-Based Tactile Sensors (VBTS) play a key role in enhancing the accuracy and efficiency of machining operations in robotic-assisted precision machining systems. Equipped with VBTS, these systems offer contact-based measurements, which are essential in machining accurate components for industries such as aerospace, automotive, medical devices, and electronics. This paper presents a novel approach to virtual prototyping of VBTS, specifically in perpendicularity measurements using Computer-Aided Design (CAD) generation of VBTS designs, Finite Element Analysis (FEA) simulations, and Sim2Real deep learning to achieve VBTS with high precision measurements. The virtual prototyping approach enables an understanding of the contact between VBTS with different designs and machined surfaces in terms of contact module shape, thickness, markers' density. Additive manufacturing was employed to fabricate the molds of VBTS contact module, followed by experimental validation of the robotic arm to confirm the effectiveness of the optimized VBTS design. The results show that deviation from the hemispherical shape reduces the data quality captured by the camera, hence increasing the prediction errors. Additionally, reducing the thickness of the contact module enhances the precision of perpendicularity measurements. Importantly increasing markers' distribution density significantly enhances the accuracy of up to 92 markers at which above it the rate of improvement becomes less pronounced. An VBTS with height of 20 mm, thickness of 2 mm, and 169 markers was found to be within the stringent perpendicularity standards of the aerospace manufacturing industry of 0.58° as a root mean square error, and 1.64° as a max absolute error around the roll and pitch axis of rotation. The established virtual prototyping methodology can be transferred to a wide variety of elastomer-based sensors.

1. Introduction

High-precision machining has gained greater attention in the last decade as it is widely used for the producing components with tight tolerances across various industries. The growing demand for high precision processes has advanced robotics as a game-changer in precision machining and as a key industry 4.0 technology [1]. The integration of cyber–physical systems with the Internet of Things (IoT), Artificial Intelligence (AI), and robotics into machining manufacturing is one of the characteristic features of Industry 4.0 enabling improved communication and collaboration, data-driven decisions, and real-time monitoring of manufacturing processes. In this context, high precision machining fits well within the paradigm of Industry 4.0, as it relies on the integration of state-of-the-art technologies to optimize manufacturing efficiency and productivity [2,3].

Advanced robotics are typically equipped with sensors, vision systems, and programming algorithms to enhance precision machining with high accuracy [4]. The integration of advanced perception technologies has gained attention in enhancing robotic-assisted precision machining processes. Typically, robots are being used for machining tasks with lower cutting force requirements, like trimming, drilling, deburring, grinding, and milling parts due to their efficiency and cost-effectiveness. The growth in the robot market is underpinned by a significant and consistent sales trend. In 2016 alone, there was a 16 percent increase in robot sales, reaching a total of 294,000 units, compared to the previous year [1]. In addition, despite the challenges posed

---

by the covid pandemic and the contraction of certain markets, there was a continuous annual increase of 12 percent in sales from 2017 to 2022. Using robots for handling objects in precision machining brings advantages. Robots automate material loading and unloading, and reducing errors. They can also handle delicate workpieces accurately, enhancing precision and preventing damage [5].

Vision-based tactile sensing (VBTS) is in particular one such technology that employs vision systems to monitor elastomer deformation upon contact with different surfaces, enabling the capture of topographic information. Compared to conventional tactile sensors, VBTS offers benefits like high spatial resolution, simple design, and minimal instrumentation requirements [6–8]. This has led to an increasing demand in developing and implementing this type of sensors to improve high precision machining processes. For example, Sunil et al. designed a VBTS system with the capability to grip two adjacent corners, facilitating subsequent actions such as folding or hanging. They created tactile perception networks to recognize held edges and estimate their positions. These networks direct a visuotactile edge grasp network, resulting in a significant success rate of 90 percent in gripping edges [9]. On the other hand, Ruan et al. introduced a VBTS that enables a robot to accurately determine the position of an object it holds. This is achieved by combining RGB cameras on the robot's palm with VBTS on its fingertips. This technology enables the robot to effectively handle diverse objects as it can estimate the object's position while holding it, eliminating the need for special setups [10].

When it comes to inspecting surface defects, Fang et al. introduced a vision tactile sensor designed to detect fabric defects while avoiding issues caused by varying and irregular dyeing patterns. The sensor also minimizes the impact of surrounding light, ensuring accurate defect detection [11]. 3D surface reconstruction offers significant benefits to precision machining processes, generating accurate three-dimensional representations of workpieces that provide valuable insights and enhance the optimization of various machining aspects [12]. In the context of GelStereo VBTS, Zhang et al.. introduced a universal Refractive Stereo Ray Tracing (RSRT) model enabling the 3D reconstruction of contact surfaces. Their model achieved less than a 0.35 mm Euclidean distance error [13]. On the other hand, Ma et al. developed a binocular visuotactile sensor (BVTS) for precise 3D deformation reconstruction of objects. Their model accounted for the refraction effects of elastomers when generating depth maps from markers. This BVTS accurately reconstructs real objects with high precision [14]. Additionally, Tanyeri was able to reconstruct surface roughness with sub-millimeter precision by developing a VBTS [15].

Perpendicularity is one of the important form tolerances in precision machining and widely used across a range of industries such as aerospace, automotive, and electronics, as evidenced by recent studies [16,17]. Drilling and deburring are essential machining processes and misaligned or non-perpendicular holes can lead to assembly difficulties, reduced load-bearing capacity, and increased stress concentrations which can lead to potential fatigue failure [18,19]. Moreover, perpendicularity of holes can also influence surface smoothness which affect the aerodynamics of the machined structures. Large assembly manufacturing may face challenges with workpieces deviating from their CAD models due to manufacturing errors [20]. Relying solely on the CAD model or 2D vision system for robotic drilling without real-time feedback on the normal direction measurements can make achieving satisfactory perpendicularity difficult [21,22]. Due to the wide use of VBTS, Zhang et al. introduced PFS 10, which is a GUI-based development tool for VBTS formulation and fabrication. This tool facilitates the manufacturing process of the VBTS for a specific task [23].

Despite VBTS being widely used to support precision machining through grasping, handling, surface inspection, positioning, and 3D reconstruction, there are only a few studies directly implementing VBTS in robot arms for precision machining. It is worth noting that only 1.4% of industrial robots were employed in machining tasks like cutting

and grinding. This emphasizes the increasing significance of integrating robots with versatile capabilities, such as VBTS in these specific tasks has been limited [24]. One study by Zaid et al. focused on developing VBTS for contact angle measurements and integrated into a deburring robotic arm and implemented for hole deburring [25]. Sajwani et al. developed TactiGraph VBTS using neuromorphic event-based cameras to predict contact angles. The developed TactiGraph sensor shows effective performance without internal illumination, leading to instrumentation and maintenance cost reduction. Experimental findings highlight TactiGraph's superior accuracy and efficiency compared to traditional VBTSs and require only 5.5 percent of the computational time of VBTS in direct comparisons [26]. Additionally, Halwani et al. introduce a groundbreaking multi-functional sensor that combines visual and tactile feedback in a single optical sensor. It improves robotic capabilities, providing vision-based tactile perception for precise localization and control [27]. Other studies confirm that machine learning tool is crucial in developing frameworks of tactile and perception algorithms to relate special features in the captured information to the tactile measurements [28,29]. Additionally, Zhang et al. were able to extract micro-level tactile features under certain lighting conditions using the developed sensor called TIRgel [30].

The limited adoption of VBTS in precision machining operations may be attributed to various factors, including complexities from existing intricate machinery and workflows [31]. Furthermore, high precision machining requires a high level of accuracy. Therefore, optimization of VBTS for achieving high-accuracy systems is essential to ensure a wider successful implementation. A VBTS comprises crucial components including a contact module in the form of an elastomer skin, sensing elements (markers), support structure, vision system, and illumination system [7,32–34]. Several VBTS designs are documented in literature and most of them employ flat or hemispherical elastomer skins, although exceptions exist, such as cylindrical tactile sensors tailored for endoscopy applications. While flat contact module are simple and easy to design and manufacture, their utility is limited due to how they interact with objects which makes them effective only when dealing with spherical or small flat objects with contact areas smaller than the sensing skin. In contrast, curved or semispherical sensing skins do not face this constraint, making them versatile for handling various shapes. While deformation data from the contact module and/or their markers are essential in training VBTS and affect their prediction performance. It is worth noting that despite the significant influence of elastomer contact module parameters such as shape, thickness, marker density, distribution, and height on the deformation behavior, a noticeable gap remains in the literature. Thereby, a systematic optimization framework is essential to establish the effect of such parameters on the performance of VBTS [35]. Wang et al. delivered a set of simulations by changing the material properties and radii aiming to numerically study the piezoresistive based tactile sensor to improve the response linearity [36]. However, VBTS necessitates a virtual based framework for developing their designs and optimize the sensors performance.

Through the literature review, it was confirmed that no studies have been conducted on virtual prototyping techniques for generating designs of VBTS, and the influence of VBTS elastomer contact module design parameters on overall VBTS performance has not been investigated. To address this gap, a novel prototyping technique were developed to investigate the impact of the design parameters on the performance obtaining the optimal configuration of design parameters, with the ultimate goal of enhancing VBTS measurements accuracy and flexibility. Tactile sensors are mainly manufactured from an elastomer material. the commonly used materials are Ecoflex, PDMS, P-595, Elastosil, and Dragon skin. The Ecoflex provides some advantages over other materials such as easy use, low cost, and good mechanical durability [37–41]. Consequently, It has been considered as the manufacturing material in this study. Thus, there is a gap in the design generation, specifications and optimization of VBTS systems for high precision machining operations. Furthermore, experiments were conducted to validate the proposed framework with a primer focus on contact pose estimation applications aiming to bridge the gap between theoretical design considerations and real-world performance.
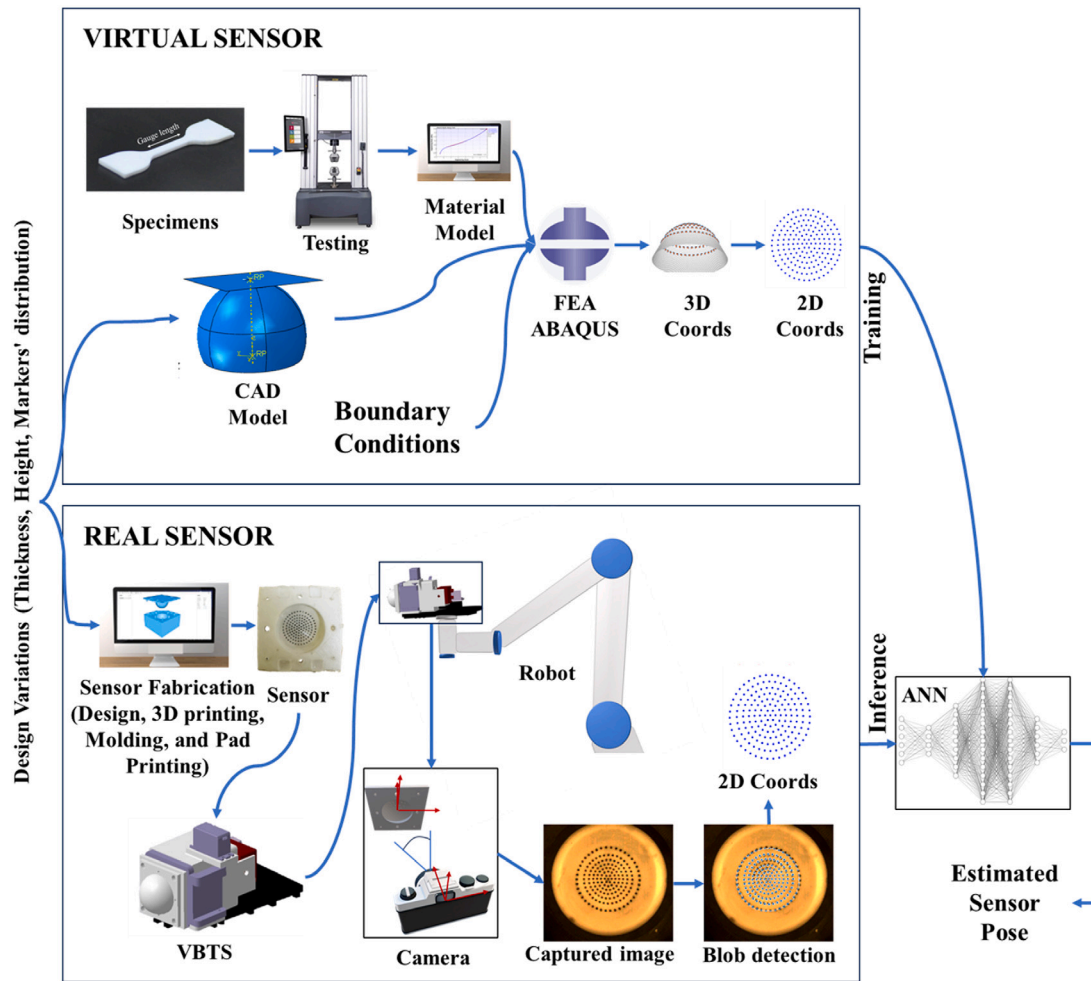
Fig. 1. Integration of virtual and real sensors in dual environments.

2. Methodology

The proposed virtual prototyping to design and optimize the contact module of VBTS for precision machining is shown in Fig. 1. The first step is to design a VBTS contact module, each exhibiting different geometrical parameters. as they are essential to interpret and analyze tactile interactions with objects. VBTS contact module is a flexible outer geometry that makes direct contact with objects. It deforms in response to applied forces or when in contact with other rigid surfaces, allowing the camera to capture data about the objects' shape, or texture. Markers are typically placed on the inner of the contact module and act as specific reference points or patterns embedded within the elastomer skin. These markers work as reference points for the sensor, allowing the tracking and measuring deformations in the skin's surface.

In the methodology presented in this study, contact modules are designed using a CAD generator platform developed using Python, considering varying contact module heights, thicknesses, and marker densities. Subsequently, the designed contact module undergoes FEA simulation using Abaqus. This simulation allows to study of the deformation of each elastomer contact module when interacts with surfaces at different perpendicularity around the pitch and roll axis. A specialized material model specific to the elastomer material is also established. The simulation evaluates the VBTS response and hence the accuracy under varying contact conditions.

To further evaluate the capabilities of the sensors, deformation and marker movement data generated from the simulations are utilized to train a deep-learning Sim2Real model. This model learns from the data and becomes capable of predicting perpendicularity based on any

future sensor readings from the real sensor. The final step includes the preparation of the contact module using 3D printing. The process starts creating molds that represents the replica of the designed sensor geometries. Afterwards, they were subjected to validation testing to compare and confirm their performance with the simulated results. The real sensor environment starts with sensor design and manufacturing. the next step is to assemble the tactile sensor and the camera into the sensor enclosure, which requires a calibration process to determine the camera intrinsics. The enclosure is fixed to the robot that controls the sensor pose. The camera captured images of the inner surfaces of the contact modules when are subjected to different deformations. Then the markers' coordinates are extracted from the captured images which represents our inference.

2.1. Fabrication of the VBTS contact module

The manufacturing of the VBTS contact module started with the creation of a CAD of the mold to replicate the required geometry. This mold was designed, considering the contact module parameters such as height, thickness, and markers counts. Using an FDM 3D printer and PLA material, the mold was fabricated. Subsequently, the Ecoflex™00-30 elastomer prepolymer was molded, cured, and then carefully peeled off from the 3D-printed mold. An additional novelty in this study was the approach to rapidly paint contact module markers. In contrast to earlier research that used plastic beads, this study introduced pad printing allowing for the precise placement and secure attachment of markers to the inner surface of the contact module in
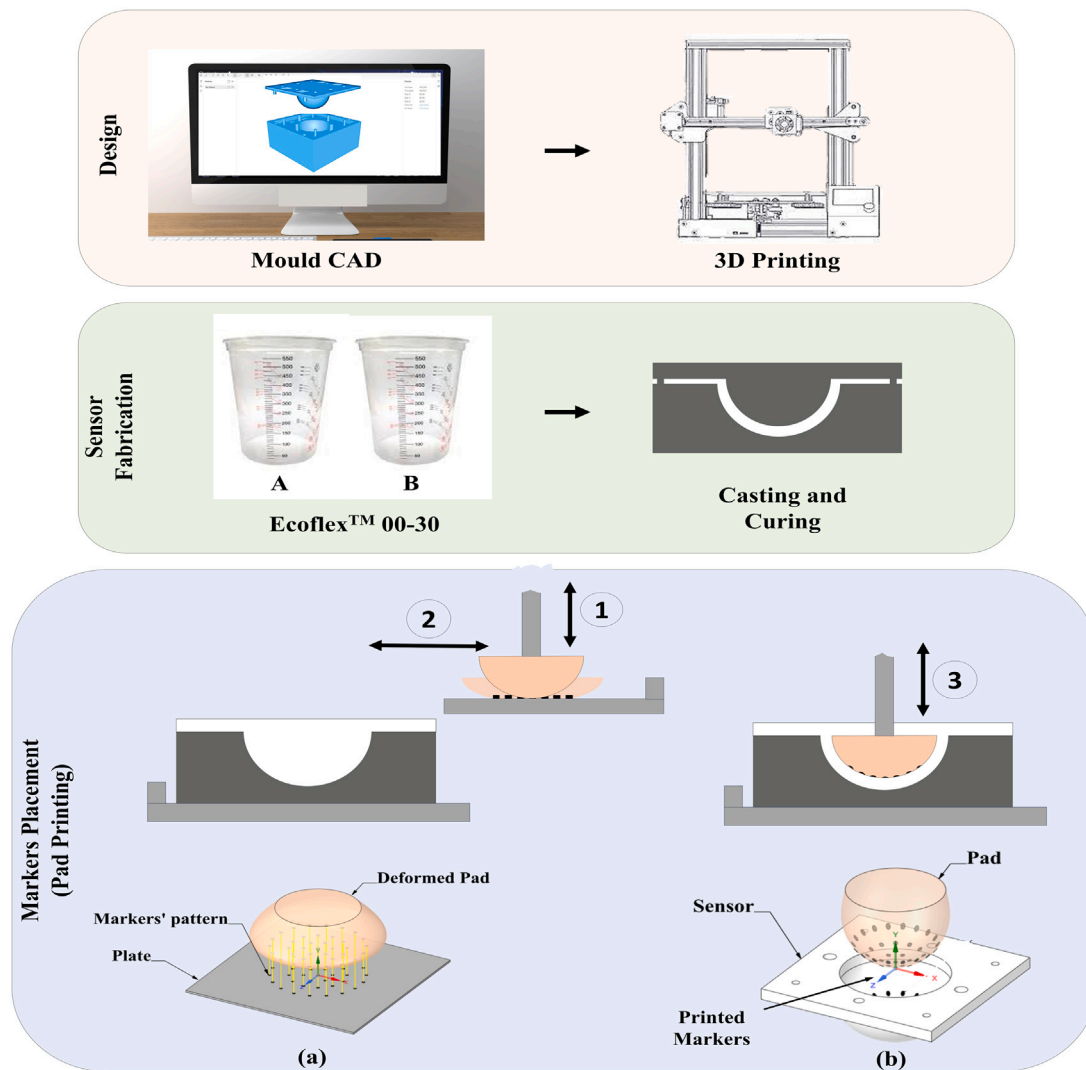
Fig. 2. A schematic diagram of the VBTS contact module development.

the exact locations. Fig. 2 provides a visual overview of the tactile sensor development process, which is divided into three distinct phases. The design process phase encompasses CAD model creation and 3D printing of the mold. The contact module fabrication phase involves the casting and curing of Ecoflex™00-30 elastomer. Finally, the pad printing (tampography) Phase details the marker transfer process, including ink application and pattern transfer to a silicone pad (step 1), followed by precise alignment and pressing onto the sensor's inner surface (steps 2 and 3).

2.2. Material properties

Ecoflex™00-30 was chosen because of its favorable physical and mechanical properties for this study. These type of elastomers are highly flexible, ductile and strong, which make it ideal for tactile sensors. The mechanical properties of Ecoflex™00-30 were measured by conducting tensile and compression tests according to ASTM standards (D412, and D395) to define the strain energy density [42–44]. The process included material preparation, testing, and calculation. While the Ecoflex™00-30 is a hyperelastic material, the material behavior is nonlinear and sensitive to environmental variables during manufacturing. The samples have been manufactured according to the standard Ecoflex™00-30 manufacturing process [45].

The specimens were fabricated through molding similar to the fabrication of the full sensor. Fig. 3 shows the CAD model of the fabricated tensile and compression test samples. Firstly, a negative shape mold or replica of the specimen was printed using a 3D printer, according to the dimensions of the tensile and compression specimens defined by the previously mentioned ASTM standard. Secondly, Ecoflex™00-30 was prepared by mixing two equal parts of (A and B) and pouring them into the mold. Thirdly, the mold containing Ecoflex™00-30 was put into a vacuum chamber for 5 min to remove any formed bubbles. Then it takes 4 h to get cured. Finally, after the specimens are cured, they are ready for the tensile and compression measurements.

2.3. Finite element analysis

VBTS designs is not a simple process due to the different design parameters available, which offers a wide design space to meet various manufacturing requirements. As a result, FEA is a useful tool as it enables a cost-effective and time-efficient assessment of different designs. In addition, the study of the available designs using FEA produces a high amount of data, which is beneficial to train the AI models in comparison with only using experimental data. Fig. 4 shows the sensor layout, where the sensor's shape was designed as a sector of a sphere with a base radius (B) of 20 mm and varying heights (H) (10 mm for hemispherical segment, 20 mm for true hemisphere, and 30 mm for spherical cap). A range of thicknesses (T) (1 mm, 2 mm, 3 mm, and 4 mm) were examined for each height. Consequently, the sensor's inner
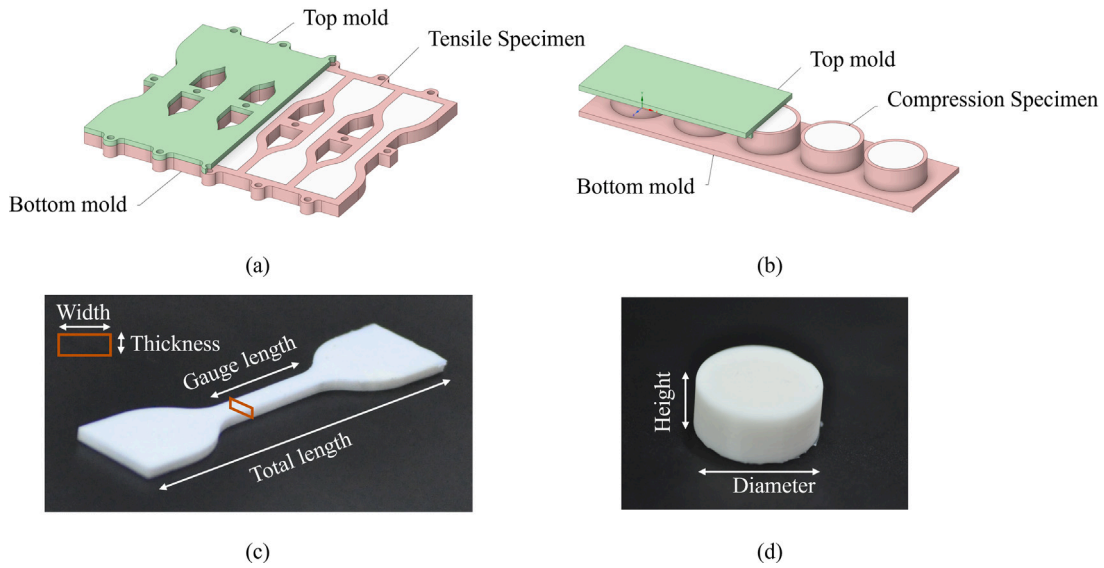
(a)

(b)

(c)

(d)

Fig. 3. CAD models of (a) tensile and (b) compression specimen molds, manufactured specimens for (c) tensile and (d) compression tests.

(a)

(b)

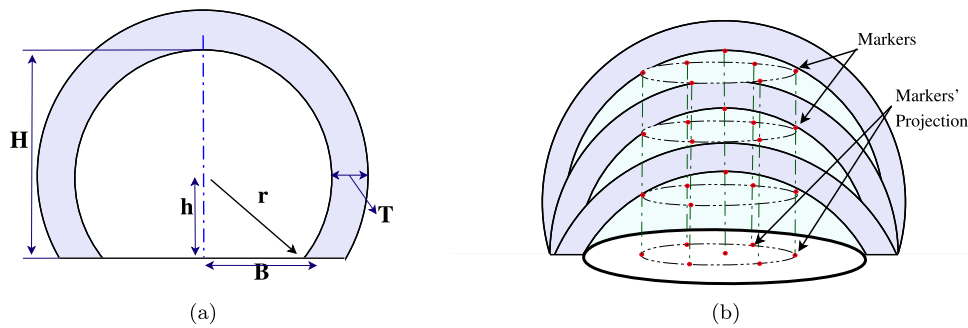**Fig. 4.** Concept of different designs; (a) Parametric shape, (b) Markers.
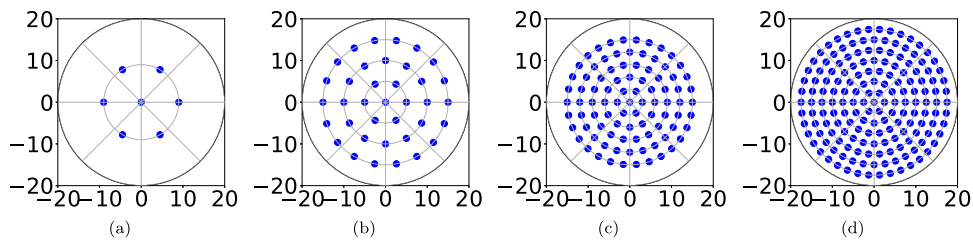

(a)

(b)

(c)

(d)

Fig. 5. Projection of markers' distributions (a) 7 markers, (b) 37 markers, (c) 91 markers, (d) 169 markers.

radii (r) were determined using Eq. (1) and found to be 12.5 mm, 20 mm, and 32.5 mm, respectively, for each height.

$$r = \frac{H^2 + B^2}{2H} \tag{1}$$

where: H is the sensor height, and B is the sensor's base radii.

The paper studied the markers counts for each design, with values of 7, 37, 91, and 169, respectively. The markers were arranged to facilitate the segmentation of the contact module into symmetric sections, with nodes corresponding to these markers symmetrically positioned in both radial and angular directions. At each level, the distribution followed a specific pattern: initially, a single marker was placed at the center. Subsequently, a circular pattern of markers was established at a specific radius, with six markers comprising the first level. For each subsequent circular pattern or level, the marker count increased by 6. Fig. 5 shows a visual representation of the 2D (projection) distribution of markers for the specified marker counts. These 2D distributions were then projected onto the curvature of the sensor to depict the marker locations in 3D.

The VBTS contact module is modeled as a shell with a spherical shape with a base diameter that remains a constant 40 mm, as depicted in Fig. 4. To model and define the positions of markers on this spherical shell, it is divided into segments by a series of planes, resulting in a collection of points at the corners of these partitions. These markers are then positioned within this group of points and assigned to a single set to keep them distinct from other elements. Fig. 6(a–c)visually represents this partitioning process for various sensor heights. For sensors with a height exceeding 20 mm, an additional partition is introduced. This extra partition serves to reduce the curvature of the sensor's surface, which, in turn, enhances the meshing process, see Fig. 6(d–f). Fixed boundary conditions in X, Y, and Z directions are assigned to the sensor base as shown in Fig. 6(g–i). Additionally, a displacement boundary condition of 8 mm is assigned to the wall to simulate the motion of the sensor to objects. This displacement occurs over 1 second, which is the time of the simulation as the displacement boundary condition is linearly proportional to the simulation time with a slope
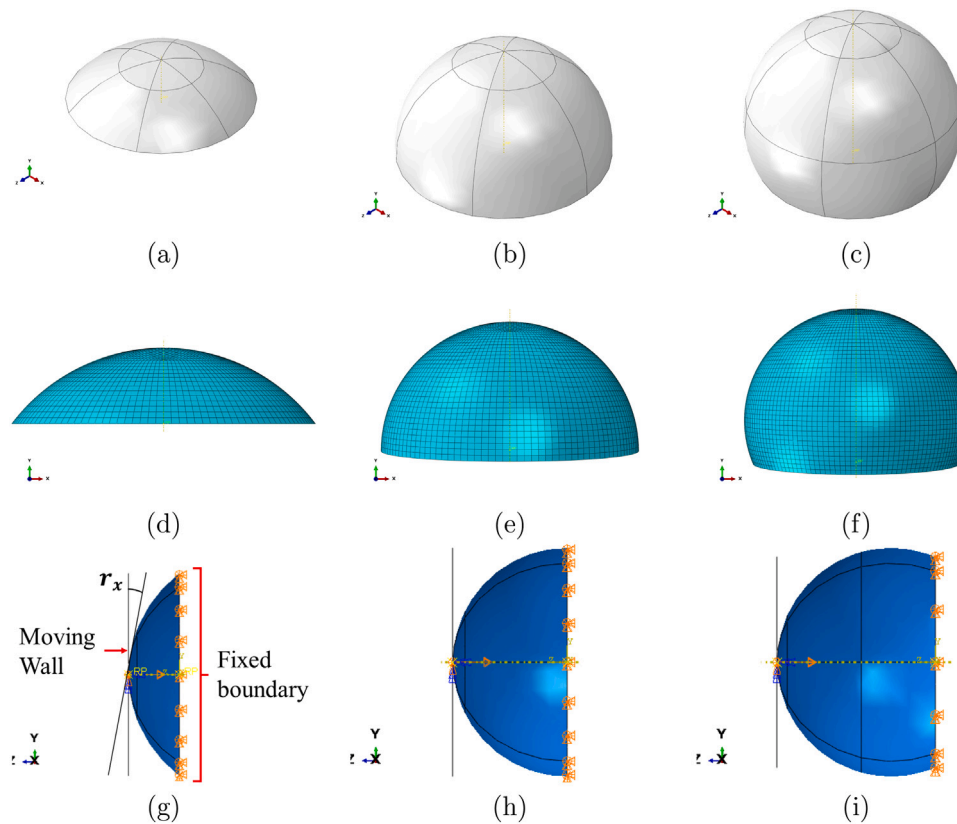
Fig. 6. The elastomer contact modules with a height of 10, 20, and 30 mm, respectively (a–c) the CAD models, (d–e) Meshing (g–i) show the boundary conditions.

of 8 mm/s. A set of configurations between the wall and the sensor is simulated to mimic the real scenarios of contact between the sensor and the objects. the variations in this set are designed by changing the two angles of inclination r_x and r_y, where r_x is shown in Fig. 6(g), and r_y in the normal direction.

3. Perpendicularity estimation using deep learning

To evaluate the accuracy of VBTS designs in predicting perpendicularity, errors between the ground truth, specifically the actual perpendicularity, and the predicted values were determined. For variation i of the tactile sensor, the sensor is simulated to make contact against a flat surface at an angle of (r_x, r_y) as shown in Fig. 7. Each simulation is carried through across as shown in Fig. 7. Across n_f frames each lasting 100 ms. The 3D positions (x, y, z) of the markers are tracked in 3D space across the n_f frames. The markers are then projected into frame coordinates $U = (u_1, u_2)$. Let $U_t^i \in \mathbb{R}^{n_m^i \times 2}$ be the coordinates at time t of each of the n_m^i markers of the ith sensor variation. Given the coordinates, U_t^i, deep learning models are used to estimate the contact angle associated with this motion of markers. The performance of these deep learning models is used as a criterion for the sensor. Thus, the performance of these deep learning models is used to assess the quality of data generated by each variation.

The models trained on the simulated data (the simulated marker coordinates in 2D U_t^i) are used without further training on the data obtained through experiments. To ensure transferability, first, the positions of the markers in the frame U_t^i are normalized between 0 and 1. This is done to account for errors arising from the positioning of the cameras with respect to the tactile sensor in the simulation compared to reality. Second, a uniformly random spatial jitter is applied with a maximum displacement of 2 pixels. This is done to account for errors in detecting markers in the real experiments hence this spatial jitter ensures better transferability of the model. Lastly, the first 2 frames of

Table 1
The hyperparameter search space S for Bayesian optimization.

Hyperparameter	Hyperparameter range
Number of layers	{2, 3, 4, 5, 6, 7}
Layer width	{32, 64, 128, 256, 512, 1024}
Dropout	{0.0, 0.5}

the simulation are dropped since these do not contain much motion and will be the same for all contact angles.

To ensure a fair comparison between different variations of the sensor, the optimization process is done over a search space, S of neural networks that map marker positions U_t^i to contact angles (r_x, r_y) is fixed across all variations. For variation i of the sensor, a search over S is conducted to find the best neural network Γ^i. The search space $S = \{\Gamma_w : \mathbb{R}^{n_m^i \times 2} \longrightarrow \mathbb{R}^2 \mid w \in \mathcal{W}\}$ of neural networks that map U_t^i to the corresponding contact angle is constructed. The search space is tabulated in Table 1.

For each variation across all contact angles, the data is split randomly into a training and validation split. To choose the best model $\Gamma^i \in S$ for each sensor variation, models are trained on the training datasets and validated over the validation set. The evaluation is done using root mean square error ($RMSE$) and the max absolute error.

$$RMSE = \sqrt{\frac{1}{n} \sum_{i=1}^{n} (y_i - \hat{y}_i)^2}. \tag{2}$$

$$\text{Max. Abs. Error} = \max_{i=1}^{n} |y_i - \hat{y}_i| \tag{3}$$

The accuracy of the VBTS was calculated as the RMSE of the elastomer modules. Better VBTS contact modules are those that yield lower $RMSE$ and $Max.Abs.Error$, shown in Eq. (3), does not exceed 2°. Bayesian optimization [46] was used with the validation $RMSE$ as the loss function over S to find the best model for each design,
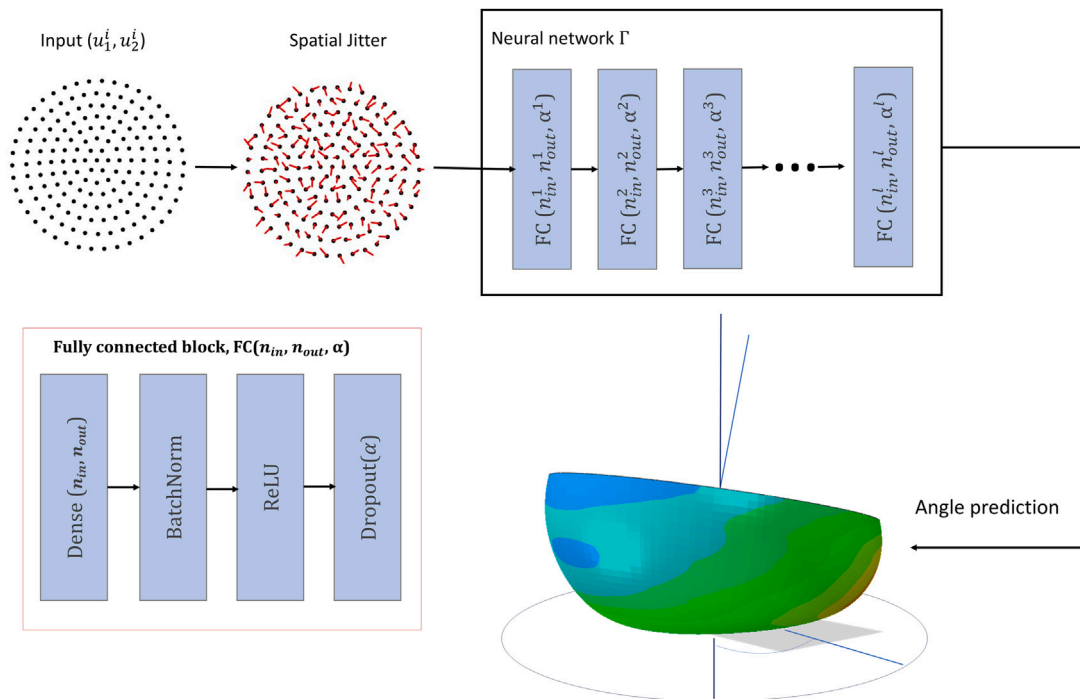
Fig. 7. Deep learning model to predict the roll and pitch angles.

see the $RMSE$ Eq. (2). For each set of hyperparameters, the model is trained 3 times to account for randomness in weight initialization. Early stopping is implemented with a patience of 75 epochs to save time while training. The Adam optimizer is used with a learning rate of 10^{-4}. The learning is decreased by a factor of 10 if the validation loss plateaus for more than 100 consecutive epochs.

4. Results and discussion

4.1. Material constitutive model

The stress–strain data of tensile and compression tests were collected experimentally at the lab room temperature because of the temperature dependence of the mechanical properties of this material [47]. Five samples for each test were fabricated and tested using Zwick/Roell Z005 testing machine of 2.5 kN load cell to collect the tensile and compression stress–strain data. Figs. 8(a) and 8(b) show the recorded stress–strain data of compression and tensile tests. The results indicate strong repeatability across all five samples, observed in both the tensile and compression tests. The tests were terminated when the strain reached 4 times the original length in the case of tensile testing and when deformation reached half of the initial length in compression testing. This limit was established considering the proposed VBTS contact module's deformation range, which falls below these limits. It can be noted that compression stress of 0.1 MPa was recorded at half of the sample's initial height, while the tensile strength measured 0.25 MPa when deformed five times its original length. Note that the manufacturer's specified ultimate strength is 1.37 MPa. PolymerFEM software is used to build the material model based on an optimization technique to optimize the strain energy function for the best coefficients of the Yeoh model [48]. Fig. 8(c) shows the comparison between the experimental data and the optimized material model, where the model extremely fits the experimental data. Table 2 shows the optimized coefficients of the Yeoh model.

The coefficients of the hyperelastic material model (Yeoh) are shown in Table 2. C_{10} represents the linear behavior at low stains, and C_{20}, and C_{30} describe the higher-order behavior. Using the provided coefficients, the Yeoh material model is defined on ABAQUS software,

Table 2
Yeoh material model coefficients.

Coefficient	C_{10}	C_{20}	C_{30}
Value	14 115.6	110.6	4.8

where all the units are considered to be basic SI units. The assembly is constructed as discussed in Section 2.3 as a shell surface with a thickness of 4 mm as shown in Fig. 4, S4R element type is utilized in the ABAQUS library. A mesh sensitivity study was carried out to find the best mesh size. Fig. 9 shows the max stress and the relative error at different numbers of elements; the relative error gets lower than 5 % at 2438 elements and mesh size of 0.005 m which represents the best number of elements and mesh size. The maximum deviation factor is kept constant of value 0.005 through the mesh study.

4.2. Deformation behavior of the contact module

The deformation behavior of the elastomer contact module affects the sensitivity and accuracy of the VBTS sensor. When the elastomer contact module contacts a rigid surface, it undergoes deformations. Firstly, it experiences compression at the point of contact, as the elastomer material flattens or conforms to the shape of the rigid surface, driven by the applied displacement. Additionally, the outer surface of the contact module undergoes deflection, causing it to deviate from its initial shape. These deformations, both surface deflection and strain are important in VBTA sensing. They enable the movements of markers on the inner surface of the elastomer contact module, allowing for the capturing the distinctive information about the rigid surface it comes into contact with. The FEA simulation model as a part of a virtual environment is designed to replicate the sensor's deformation behavior. Simulation outputs of the different CAD designs are then processed by a virtual camera model to produce results similar to real-world experiments. One primary objective of this simulation is to generate a substantial dataset representing various perpendicularity scenarios for training the deep learning models, as explained in Fig. 1.

Fig. 10 presents an example from one of the FEA datasets, depicting the stress distribution and deformations observed in various contact
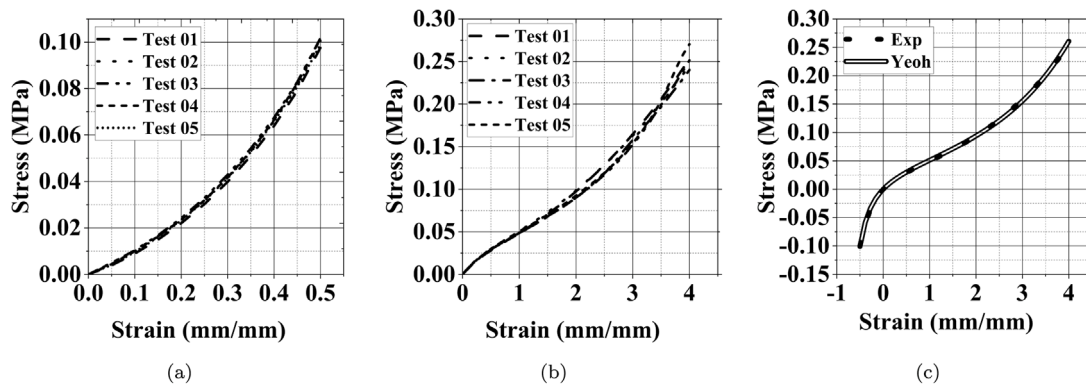
Fig. 8. (a) Compression test, (b) tensile test, (c) Experimental results with the optimized Material model.
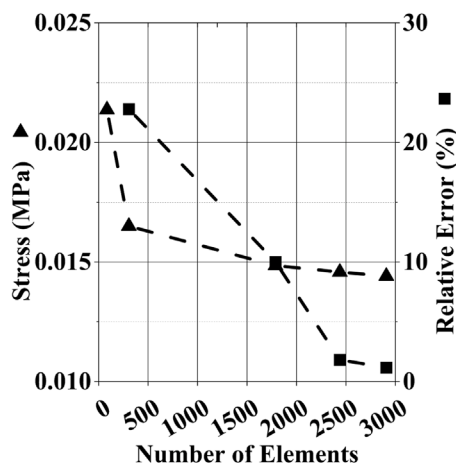

Fig. 9. An example of the Mesh sensitivity analysis.

module designs when equipped with two distinct contact module thicknesses: one using a 2 mm thickness and the other using a 1 mm thickness. In Fig. 9(a–c), it is evident that the observed variations in maximum stresses among elastomer contact modules can be attributed to their respective shapes. The elastomer contact module with a 10 mm height, designed in a hemispherical segment shape, exhibits the highest stress levels due to stress concentration at the apex of the dome-like structure. Following closely is the 20 mm-height contact module with a similar hemispherical design, where the increased height allows for better load distribution but still results in elevated stress levels. In contrast, the 30 mm-height contact module with a spherical cap shape displays the lowest stresses. The spherical cap shape distribution applies loads more evenly over the curved surface, while the increased height further enhances load distribution, resulting in the lowest stress concentrations in the dataset. Applying constant displacement at the apex of the contact module results in a localized, concentrated load at that point. This concentrated load, in turn, leads to high stresses in the immediate vicinity of the apex. Since apex is the highest curvature point, stress concentration is particularly the highest.

On the other hand, constraining the dome shape from the edges means that the outer perimeter of the dome is fixed. This boundary condition can affect stress distribution by restricting the displacements at the edges. Consequently, stress concentration is not confined solely to the apex but extends to an annular region just below it. It is important to note that the maximum stresses observed in these designs are notably lower than the maximum stresses exhibited by Ecoflex™00-30, as illustrated in Fig. 10. Furthermore, in Fig. 10(d–f), the contact module deformation is presented for a 2 mm thickness, while Fig. 10(g–i) depicts deformations for a 1 mm thickness. When these diverse designs with varying thicknesses and shapes interact with rigid surfaces, distinct deformation behaviors emerge. It becomes evident that contact modules with a hemispherical design exhibit the most substantial deformations in comparison to hemispherical segments or spherical caps. Additionally, with a thicker contact module thickness of 2 mm, most outer surfaces conform to the contour of the rigid surface. In contrast, the elastomer contact module with a 1 mm thickness undergoes significant deformation, often resulting in apex regions inverting and propagating in different directions, particularly pronounced when using thinner elastomers and also when contact occurs at steeper inclination angles as shown from other data sets. This behavior can be attributed to the considerable deformation experienced and the resulting low local directional stiffness of the elastomer.

After collecting simulation data set that tracked the motion of markers, where the markers' locations were represented as the movement of nodes, various designs of the elastomer contact module were explored. The aim was to understand how contact module designs affects the markers movement. This analysis is summarized in the following 3D graphs that depict the influence of these design variables on the average distance traveled by each marker, with different counts of markers. Fig. 11 provides a visual representation of the results. It reveals that elastomer contact module designs with seven markers exhibited the shortest traveled distance per marker, while designs with 169 markers showed the greatest average distance covered by each marker. Notably, minimal variation was observed when employing elastomer contact modules with 37, 96, and 169 markers, all exceeding 1 mm on average distance. Considering the influence of the dome shape and height, it was observed that elastomer contact modules designed with a hemispherical shape and a height of 20 mm generally outperformed other designs, producing the greatest average distance covered by each marker. Conversely, elastomer module designs with either a hemispherical segment shape or a spherical cap shape performed less favorably across most used thicknesses, which is in agreement with Fig. 10. Furthermore, the thickness that affects the average distance traveled by each marker was found to be dependent on the shape of the contact module and the number of markers used. In general, when utilizing a hemispherical segment shape (height = 10 mm), there was a minimal increase or a stable average distance traveled by each marker with increased thickness. For designs with hemispherical and spherical cap shapes, a rapid increase in the average distance traveled by each marker was observed when thickness was increased from 1 mm to 2 mm, followed by a more gradual increase with further thickness increments.

4.3. Sim2Real and VBTS accuracy

The above results confirmed the effects of the contact module's design on markers movement. Following that, the Sim2Real study was carried out to assess VBTS accuracy in measuring the perpendicularity of machined surfaces around the roll and pitch axis. This was driven by
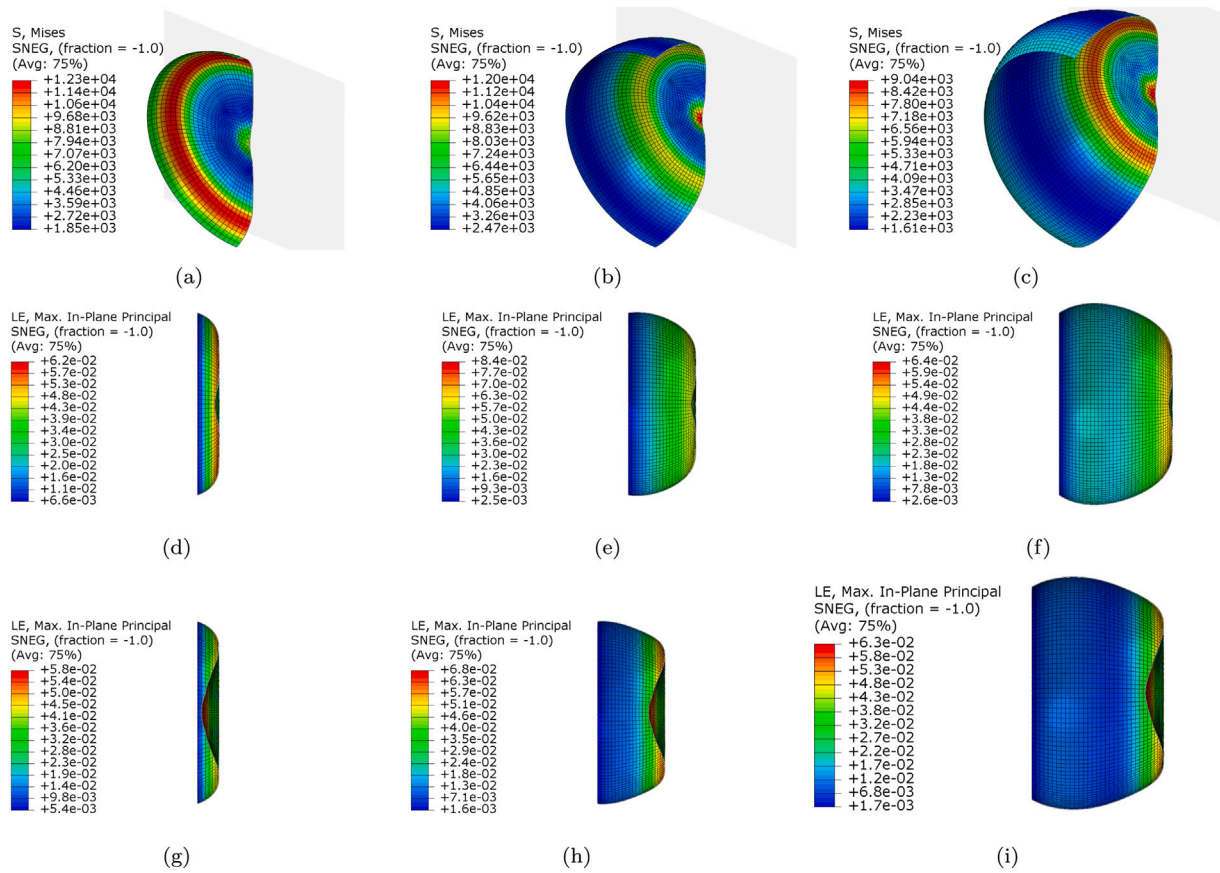
Fig. 10. An example of FEA showing stresses for (a) hemispherical segment, $t = 2$ mm (b) hemispherical, $t = 2$ mm (c) spherical cap, $t = 2$ mm; Deformation for (d) hemispherical segment, $t = 2$ mm, (e) hemispherical, $t = 2$ mm, (f) spherical cap, $t = 2$ mm, (g) hemispherical segment, $t = 1$ mm, (g) hemispherical, $t = 1$ mm, (g) spherical cap, $t = 1$ mm.
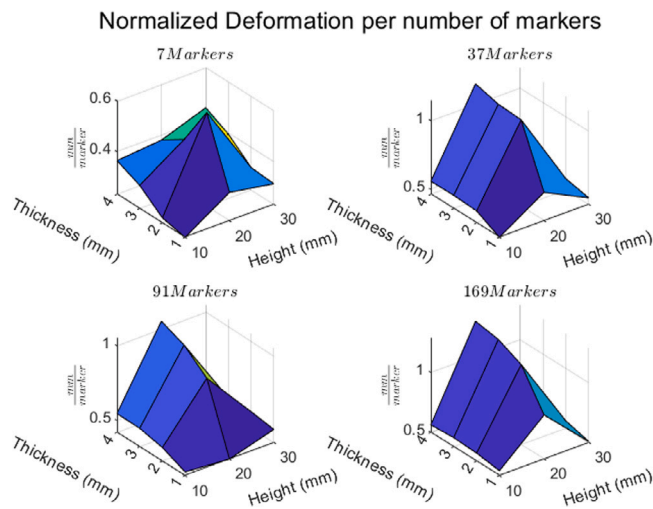

Fig. 11. Average distance traveled by each marker.

the observed deviations in marker movements and their reliance on the VBTS design. These findings are visually depicted in Fig. 12, presenting a heatmap that illustrates the impact of various contact module designs on two important VBTS accuracy metrics: Root Mean Square Error ($RMSE$) and Maximum Absolute Error ($Max.Abs.Error$). The heatmap visually represents the performance of various contact module designs, each characterized by their shapes, including hemispherical segments, hemispheres, or spherical caps, combined with various thicknesses and marker counts. The data base used to create the heatmap services

as a specification grid for each design, enabling easy access to their individual performance metrics. Each contour in the heatmap provides relevant data for each VBTS design.

Examining the figure, it becomes evident that an increase in the number of markers within the elastomer contact module leads to a noticeable improvement in the accuracy of the VBTS, as reflected by the reductions in $RMSE$ and $Max.Abs.Error$. This enhancement is clearly depicted by the larger, darker areas on the plot. The optimal level of accuracy is achieved when utilizing 169 markers, resulting in the lowest $RMSE$ of 0.3° and $Max.Abs.Error$ of 0.8° for the hemispherical design with a 2 mm thickness. Those metrics represent the model performance on the simulation data, in other words, the quality of each design. Upon analyzing the influence of the dome shape, elastomer contact modules designed with a hemispherical shape and 20 mm height consistently outperformed other designs. This improvement is evident, as better accuracy tends to concentrate around the 20 mm height in all the figures. Furthermore, this enhanced accuracy, depicted by the central dark region, expands as the marker count increases.

To validate the accuracy of the virtual prototyping methodology, an experimental setup was designed to evaluate the behavior and validate precision of the optimized VBTS. This experimental elastomer contact module was designed as a hemispherical shape of 20 mm in height, 2 mm in thickness, and equipped with 169 markers. The experimental setup, depicted in Fig. 13, was established to gather experimental data. This setup involved a camera (DAVIS 346) that captured images of the inner surface of the sensor, where the markers were imprinted. The markers were applied to the elastomer contact module using pad printing, as previously discussed, and are shown in the figure as rounded black dots on the inner surface of the contact module. A blob detection algorithm was employed to locate and identify these markers within the captured images, allowing us to extract the coordinates of their centers.
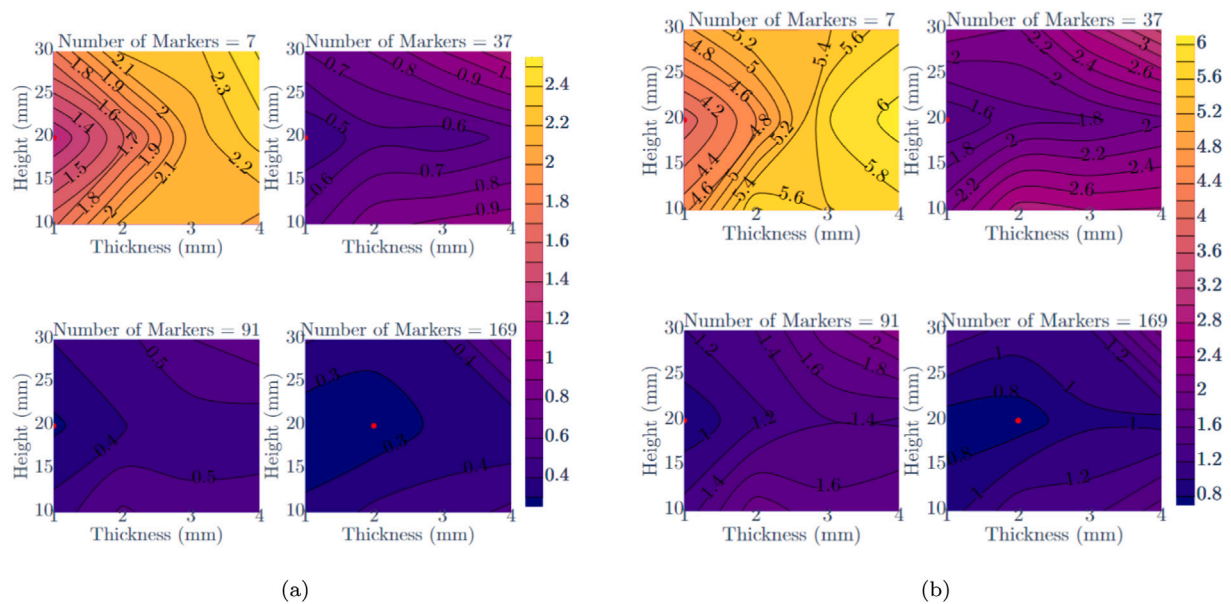
(a)   (b)

Fig. 12. Heat map of the accuracy of various VBT designs in terms of (a) Root Mean Square Error and (b) Max Absolute Error.
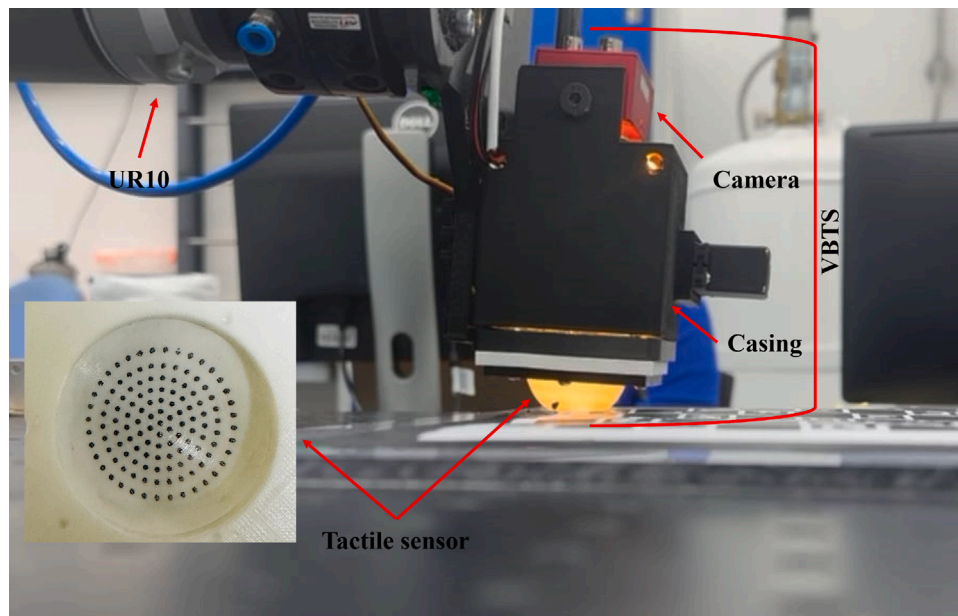

Fig. 13. The fabricated optimized VBTS design in operation.

To enhance VBTS accuracy and mitigate the influence of outliers, and centralization, normalization techniques were applied. The marker distribution formed a nearly circular pattern predominantly around the center of the image. Therefore, centralizing the data about the center of the image was essential to ensure a balanced distribution around zero. Additionally, since the coordinates were extracted, the data range had to align with the image dimensions, which were 346×260 pixels in the X and Y directions. Thus, the data was normalized, scaling it to range from -1 to 1. The design of the sensor significantly influences its performance across different contact scenarios. The movements and deformations of the markers are crucial, as they contribute to the overall deformation of the tactile surface. Therefore, the quality of these tactile features is directly linked to the sensor's design. These tactile features, which are represented by the markers, are then translated into tactile measurements, such as perpendicularity measurements. In the aerospace industry, tasks like deburring, drilling, and welding require

precise perpendicularity. Thus, the scenario of perpendicularity measurements entails a deburring machining process with measurements taken by a collaborative robot (cobot), as illustrated in Fig. 14.

The figure depicts the VBTS setup mounted on a cobot arm alongside a deburring tool. The workpiece is varied to assess different perpendicularity angles and validate the VBTS measurements. After collecting the experimental data, the performance of the model, previously trained on simulation data from various designs, was evaluated. Table 3 lists the performance metrics, including the root mean square error ($RMSE$), mean absolute error (MAE), maximum absolute error, and standard deviation. These metrics are tabulated along with the roll and pitch angles of contact and the depth of contact. Roll and pitch angles represent rotations about the X and Y axes, respectively, while the depth is measured with respect to the Z axis. The tabulated results exhibit a good agreement between simulation and experimental results, confirming the robustness of the proposed virtual prototyping
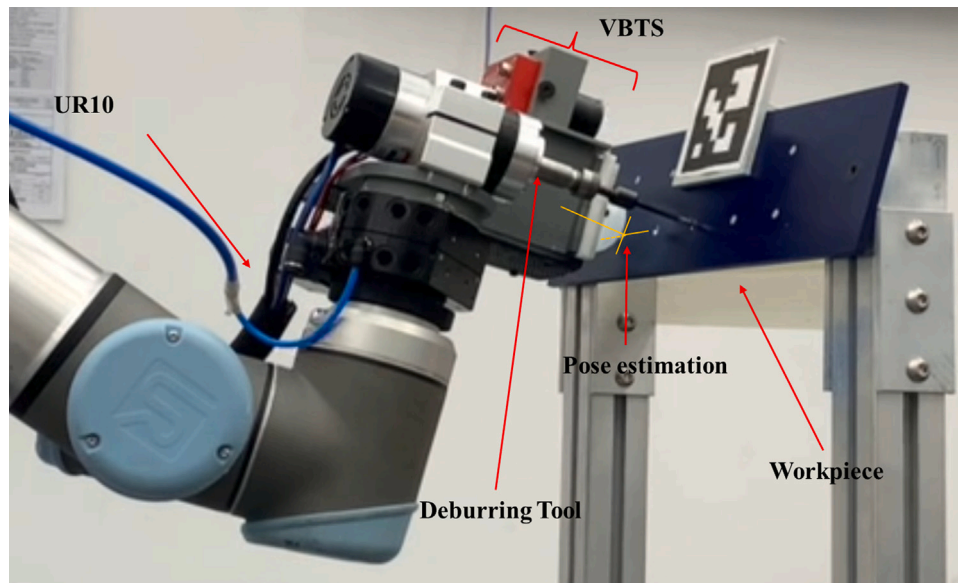
Fig. 14. VBTS in operation for normality assurance in deburring process.

Table 3
Performance metrics of the optimal sensor design for contact pose estimation.

Metric	Roll	Pitch	Depth
$RMSE$	0.58°	0.57°	1.00 mm
MAE	0.49°	0.47°	1.00 mm
$Max.Abs.Error$	1.62°	1.64°	1.40 mm
SD	0.54°	0.49°	0.16 mm

method for roll and pitch measurements. The predicted $RMSE$ values for perpendicularity and depth were approximately 0.58° for roll, 0.57° for pitch, and 1 mm for depth, respectively. In a comparative study by Yang et al. (2024) investigating robotic grippers rotating at different angles, higher angular and transitional $RMSEs$ of 5.03° and 2.41 mm were achieved using a pair of VBTSs for contact pose estimation via the Sim2Real approach [49], though without the use of FEA. The high precision model's presented in this paper is within the aerospace precision machining standard of perpendicularity form tolerance with low values in roll and pitch axis, indicating not only accurate predictions but also highlighting the role of optimal design configurations of VBTS elastomer contact module such as the shape, marker counts, thickness, and the integration of pad printing technology addressing marker printing disparities between virtual and physical sensors is important in improving the accuracy of VBTS.

5. Conclusion

This study proposed a novel virtual prototyping methodology to design elastomer contact modules for VBTS applications. The primary aim was to address the challenge of maintaining tight perpendicularity tolerance of precision machining tasks, such as drilling and deburring, as non-perpendicular holes can lead to reduced load-bearing capacity, and potential fatigue failure in aerospace structure. The proposed methodology implemented CAD design generation, FEA, deep learning models, Sim2Real, and additive manufacturing to create VBTS designs. Furthermore, the established relation between VBTS contact module shape, thickness, markers' counts on VBTS accuracy. The study involves the development and validation of the elastomer material constitutive model which was used in the FEA simulation. The results showed that the hemispherical shape represents an optimal shape with improved VBTS accuracy. Additionally, increasing the number of markers and

reducing the thickness improved the sensor sensitivity and accuracy. The study also identified a high precision VBTS design with specific parameters: a 20 mm height, 2 mm thickness, and 169 markers. This design went through an experimental validation and met the aerospace perpendicularity standards, achieving a low root mean square error of 0.58°. Additionally, the results provide a specification grid for each of the developed VBTS design, allowing easy access to their individual accuracy metrics. This grid can be used as a detailed reference for evaluating the suitability of VBTS designs concerning their shape, thickness, and marker counts. The introduced virtual prototyping approach not only contributes to the advancement of precision manufacturing by enhancing the accuracy of VBTS but also opens new possibilities for various types of tactile sensors employing elastomer contact modules across a wide range of applications.

CRediT authorship contribution statement

Islam Mohamed Zaid: Writing – original draft, Visualization, Validation, Methodology, Investigation. **Hussain Sajwani:** Writing – original draft, Visualization, Software, Methodology, Formal analysis. **Mohamad Halwani:** Writing – original draft, Visualization, Validation, Methodology. **Hany Hassanin:** Writing – review & editing, Writing – original draft, Visualization, Supervision, Investigation, Formal analysis, Conceptualization. **Abdulla Ayyad:** Writing – review & editing, Writing – original draft, Supervision, Methodology. **Laith AbuAssi:** Conceptualization, Investigation. **Fahad Almaskari:** Writing – review & editing, Supervision, Methodology, Conceptualization. **Yarjan Abdul Samad:** Writing – review & editing, Supervision, Formal analysis. **Abdulqader Abusafieh:** Writing – review & editing, Supervision, Resources, Funding acquisition. **Yahya Zweiri:** Writing – review & editing, Supervision, Resources, Project administration, Funding acquisition, Conceptualization.

Declaration of competing interest

The authors of this article declare that they have no conflicts of interest regarding the publication if this manuscript.

Data availability

Data will be made available on request.

Declaration of generative AI

Acknowledgments

Appendix A. Supplementary data

Supplementary material related to this article can be found online at https://doi.org/10.1016/j.sna.2024.115469.

References

[1] A. Verl, A. Valente, S. Melkote, C. Brecher, E. Ozturk, L.T. Tunc, Robots in machining, CIRP Ann 68 (2) (2019) 799–822.

[2] M. Ryalat, H. ElMoaqet, M. AlFaouri, Design of a smart factory based on cyber-physical systems and Internet of Things towards Industry 4.0, Appl. Sci. 13 (4) (2023) 2156.

[3] V.B. Neto, C. Marques, A. Frizera-Neto, A.G. Leal-Junior, FBG-Based Sensing System to Improve Tactile Sensitivity of Robotic Manipulators Working in Unstructured Environments. Available at SSRN 4369590.

[4] M. Javaid, A. Haleem, R.P. Singh, R. Suman, Substantial capabilities of robotics in enhancing industry 4.0 implementation, Cogn. Robotics 1 (2021) 58–75.

[5] R.N. Albustanji, S. Elmanaseer, A.A. Alkhatib, Robotics: Five senses plus one—An overview, Robotics 12 (3) (2023) 68.

[6] J.-Y. Lin, X.-W. Lee, M.-C. Hsieh, C.-O. Chang, High-angular-sensitivity total-internal-reflection heterodyne interferometry for small displacement measurements, Sensors Actuators A 277 (2018) 163–168.

[7] W. Yuan, S. Dong, E.H. Adelson, Gelsight: High-resolution robot tactile sensors for estimating geometry and force, Sensors 17 (12) (2017) 2762.

[8] S. Zhang, Z. Chen, Y. Gao, W. Wan, J. Shan, H. Xue, F. Sun, Y. Yang, B. Fang, Hardware technology of vision-based tactile sensor: A review, IEEE Sens. J. (2022).

[9] N. Sunil, S. Wang, Y. She, E. Adelson, A.R. Garcia, Visuotactile affordances for cloth manipulation with local control, in: Conference on Robot Learning, PMLR, 2023, pp. 1596–1606.

[10] W. Ruan, W. Zhu, K. Wang, Q. Lu, W. Yeh, L. Luo, C. Su, Q. Wang, Vision-tactile fusion based detection of deformation and slippage of deformable objects during grasping, in: International Conference on Cognitive Systems and Signal Processing, Springer, 2022, pp. 593–604.

[11] B. Fang, X. Long, Y. Zhang, G. Luo, F. Sun, H. Liu, Fabric defect detection using vision-based tactile sensor, 2020, arXiv preprint arXiv:2003.00839 0–10.

[12] W.-C. Shi, J.-M. Zheng, Y. Li, X.-B. Li, Three-dimensional reconstruction method for machined surface topography based on gray gradient constraints, Appl. Sci. 9 (3) (2019) 591.

[13] C. Zhang, S. Cui, S. Wang, J. Hu, Y. Huangfu, B. Zhang, High-precision 3D reconstruction study with emphasis on refractive calibration of GelStereo-type sensors, Sensors 23 (5) (2023) 2675.

[14] H. Ma, J. Ji, K.-M. Lee, Effects of refraction model on binocular visuotactile sensing of 3-D deformation, IEEE Sens. J. 22 (18) (2022) 17727–17736.

[15] B.T. Turkey, Image processing based tactile tactical sensor development and sensitivity determination to extract the 3D surface topography of objects, Sensors Actuators A 358 (2023) 114415.

[16] M. Aamir, A. Sharif, M.Z. Zahir, K. Giasin, M. Tolouei-Rad, Experimental assessment of hole quality and tool condition in the machining of an aerospace alloy, Machines 11 (7) (2023) 726.

[17] Y. Fan, J. Huang, Y. Zhang, N. Huang, Q. Bi, Y. Wang, Improvement in hole-pose error for aerospace drilling applications based on Hermite surface reconstruction and manifold error similarity, Precis. Eng. 81 (2023) 22–35.

[18] L. Yu, Y. Zhang, Q. Bi, Y. Wang, Research on surface normal measurement and adjustment in aircraft assembly, Precis. Eng. 50 (2017) 482–493.

[19] Y. Zhang, Q. Bi, L. Yu, Y. Wang, Online adaptive measurement and adjustment for flexible part during high precision drilling process, Int. J. Adv. Manuf. Technol. 89 (2017) 3579–3599.

[20] L. Yu, Q. Bi, Y. Ji, Y. Fan, N. Huang, Y. Wang, Vision based in-process inspection for countersink in automated drilling and riveting, Precis. Eng. 58 (2019) 35–46.

[21] Y. Gao, D. Wu, Y. Dong, X. Ma, K. Chen, The method of aiming towards the normal direction for robotic drilling, Int. J. Precis. Eng. Manuf. 18 (2017) 787–794.

[22] W. Zhu, B. Mei, G. Yan, Y. Ke, Measurement error analysis and accuracy enhancement of 2D vision system for robotic drilling, Robot. Comput.-Integr. Manuf. 30 (2) (2014) 160–171.

[23] S. Zhang, Y. Sun, F. Sun, Y. Yang, B. Fang, PFS 1.0: A development tool applied to vision-based tactile sensor process formulation and fabrication, Sensors Actuators A 367 (2024) 115090.

[24] C. Taesi, F. Aggogeri, N. Pellegrini, COBOT applications—Recent advances and challenges, Robotics 12 (3) (2023) 79.

[25] I.M. Zaid, M. Halwani, A. Ayyad, A. Imam, F. Almaskari, H. Hassanin, Y. Zweiri, Elastomer-based visuotactile sensor for normality of robotic manufacturing systems, Polymers 14 (23) (2022) 5097.

[26] H. Sajwani, A. Ayyad, Y. Alkendi, M. Halwani, Y. Abdulrahman, A. Abusafieh, Y. Zweiri, TactiGraph: An asynchronous graph neural network for contact angle prediction using neuromorphic vision-based tactile sensing, Sensors 23 (14) (2023) 6451.

[27] M. Halwani, A. Ayyad, L. AbuAssi, Y. Abdulrahman, F. Almaskari, H. Hassanin, A. Abusafieh, Y. Zweiri, A novel vision-based multi-functional sensor for normality and position measurements in precise robotic manufacturing, 2023, Available at SSRN 4360666, 0–10.

[28] S. Tsuji, T. Kohama, Using a convolutional neural network to construct a pen-type tactile sensor system for roughness recognition, Sensors Actuators A 291 (2019) 7–12.

[29] V. Corsino, V. Ruiz-Díez, J.M. Gilpérez, M. Ramírez-Palma, J.L. Sánchez-Rojas, Machine learning techniques for the estimation of viscosity and density of aqueous solutions in piezo-actuated 3D-printed cells, Sensors Actuators A 363 (2023) 114694.

[30] S. Zhang, Y. Sun, J. Shan, Z. Chen, F. Sun, Y. Yang, B. Fang, Tirgel: A visuo-tactile sensor with total internal reflection mechanism for external observation and contact detection, IEEE Robot. Autom. Lett. (2023).

[31] U.H. Shah, R. Muthusamy, D. Gan, Y. Zweiri, L. Seneviratne, On the design and development of vision-based tactile sensors, J. Intell. Robot. Syst. 102 (2021) 1–27.

[32] D. Zhao, F. Sun, An accurate positioning method for robotic manipulation based on vision and tactile sensors, in: Cognitive Systems and Signal Processing: 5th International Conference, ICCSIP 2020, Zhuhai, China, December 25–27, 2020, Revised Selected Papers 5, Springer, 2021, pp. 621–631.

[33] V. Kakani, X. Cui, M. Ma, H. Kim, Vision-based tactile sensor mechanism for the estimation of contact position and force distribution using deep learning, Sensors 21 (5) (2021) 1920.

[34] M. Li, T. Li, Y. Jiang, Marker displacement method used in vision-based tactile sensors—From 2D to 3D-A review, IEEE Sens. J. (2023).

[35] H. Can, P. Svec Jr., J. Bydzovsky, P. Svec Sr., H. Sözeri, U. Topal, Systematic optimization of the sensing properties of ring-core fluxgate sensors with different core diameters and materials, Sensors Actuators A 255 (2017) 94–103.

[36] Z.-P. Wang, H. Yao, H.H. See, W. Yang, B.C.K. Tee, Z. Liu, Tactile sensory response prediction and design using virtual tests, Sensors Actuators A 360 (2023) 114571.

[37] D.J. Sut, P. Sethuramalingam, Soft manipulator for soft robotic applications: a review, J. Intell. Robot. Syst. 108 (1) (2023) 10.

[38] T.-D. Nguyen, J.S. Lee, Recent development of flexible tactile sensors and their applications, Sensors 22 (1) (2021) 50.

[39] Y. Chen, J. Lin, X. Du, B. Fang, F. Sun, S. Li, Non-destructive fruit firmness evaluation using vision-based tactile information, in: 2022 International Conference on Robotics and Automation, ICRA, IEEE, 2022, pp. 2303–2309.

[40] I. Andrussow, H. Sun, K.J. Kuchenbecker, G. Martius, Minsight: A fingertip-sized vision-based tactile sensor for robotic manipulation, Adv. Intell. Syst. 5 (8) (2023) 2300042.

[41] H. Sun, K.J. Kuchenbecker, G. Martius, A soft thumb-sized vision-based sensor with accurate all-round force perception, Nat. Mach. Intell. 4 (2) (2022) 135–145.

[42] L. Marechal, P. Balland, L. Lindenroth, F. Petrou, C. Kontovounisios, F. Bello, Toward a common framework and database of materials for soft robotics, Soft Robotics 8 (3) (2021) 284–297.

[43] W. Small, M.A. Pearson, W.A. Jensen, ASTM D395 Short-Term Compression Set of Solid (Non-Porous) Siloxanes: SE 1700, Sylgard 184, and" New" M9787, Tech. Rep., Lawrence Livermore National Lab.(LLNL), Livermore, CA (United States), 2015.

[44] I. Abubakar, P. Myler, E. Zhou, Constitutive modelling of elastomeric seal material under compressive loading, Model. Numer. Simul. Mater. Sci. (2016) 28–40, (Accessed 11 April 2023).

[45] Ecoflex, Ecoflex™ 00-30 Product Information | Smooth-On, Inc., 2023, URL https://www.smooth-on.com/products/ecoflex-00-30/. (Accessed 11 April 2023).

[46] T. O'Malley, E. Bursztein, J. Long, F. Chollet, H. Jin, L. Invernizzi, et al., KerasTuner, 2019, URL https://github.com/keras-team/keras-tuner.

[47] Z. Liao, M. Hossain, X. Yao, Ecoflex polymer of different Shore hardnesses: Experimental investigations and constitutive modelling, Mech. Mater. 144 (2020) 103366, http://dx.doi.org/10.1016/j.mechmat.2020.103366.

[48] J. Lavazza, M. Contino, C. Marano, Strain rate, temperature and deformation state effect on Ecoflex 00-50 silicone mechanical behaviour, Mech. Mater. 178 (2023) 104560, http://dx.doi.org/10.1016/j.mechmat.2023.104560, URL https://www.sciencedirect.com/science/article/pii/S0167663623000066.

[49] S. Yang, W.D. Kim, H. Park, S. Min, H. Han, J. Kim, In-hand object classification and pose estimation with sim-to-real tactile transfer for robotic manipulation, IEEE Robot. Autom. Lett. 9 (1) (2023) 659–666.

Islam Mohamed Zaid earned his BSc. in Mechanical Engineering from Zagazig University, Egypt, in 2018. He is currently pursuing his MSc. in Aerospace Engineering at Khalifa University, Abu Dhabi, UAE. His research interests include neuromorphic vision, tactile sensing, soft robotics, Artificial Intelligence, and numerical simulations.

Hussain Sajwani received his B.Sc. in Applied Mathematics and Statistics from Khalifa University, UAE Abu Dhabi. He is currently working in the advanced research and innovation center at Khalifa University, Abu Dhabi, UAE. His research interests include event-based vision, neuromorphic computing, and tactile sensing.

Mohamad Halwani received his Msc. degree in Mechanical Engineering from Khalifa University, UAE, in 2021. He is currently pursuing PhD. degree in engineering with focus on Robotics at Khalifa University, UAE. His research interests include event-based vision, vision-based tactile sensing and its applications in robotic manufacturing and manipulation.

Hany Hassanin, a reader and engineering research lead, earned his Ph.D. in mechanical engineering from the University of Birmingham. He has since held academic positions at Kingston University and the University of Liverpool. Dr. Hassanin's research focuses on advanced manufacturing, particularly in aerospace, biomedical engineering, and water treatment, employing technologies such as additive manufacturing and nanotechnology. He has collaborated on projects with industry and published over 120 publications and patents.

Abdulla Ayyad received the M.Sc. degree in electrical engineering from The University of Tokyo, in 2019. He conducted research with the Spacecraft Control and Robotics Laboratory, The University of Tokyo. He is currently a Research Associate with the Advanced Research and Innovation Center (ARIC), Khalifa University, working on several robot autonomy projects. His current research interests include the application of AI in the fields of perception, navigation, and control.

Laith AbuAssi received his bachelor's degree in Mechatronics Engineering from the Hashemite University, Jordan in 2012. He was a Research and Development Engineer and Mechatronics Systems Unit Supervisor with King Abdullah Design and Development Bureau (KADDB), gaining +12 years of experience in the fields of aerospace, defense, and military systems. He is currently a senior researcher with the Advanced Research and Innovation Center (ARIC) and the Aerospace Department at Khalifa University, UAE. His research activities focus on the hardware and software R&D of robotic systems that include space rovers, weapon stations, medical robotics, industrial 4.0, IoT, machine learning, and AI.

Dr. Fahad Almaskari, a Mechanical Engineering Ph.D. graduate from the University of Manchester (2010), transitioned from senior roles in Abu Dhabi Gas Companies to academia. Serving as Assistant Professor at The Petroleum Institute (2011–2017) and presently at Khalifa University, he specializes in Aerospace Engineering. Dr. Almaskari's expertise lies in Finite Element Analysis, with a focus on advanced materials like composites and lattice structures. Passionate about robotics, he explores its applications in manufacturing and advanced technologies.

Dr Yarjan Abdul Samad is an Assistant Professor of Aerospace Engineering at Khalifa University, UAE and a Senior Research Associate and Senior Teaching Fellow at The University of Cambridge. He is also the Chief Technology Advisor to a climate change company called Levidian based out of Cambridge, UK, which is transforming waste gas resources to graphene and hydrogen. His research work is based on developing graphene & 2d materials-based technologies for Space and Aerospace. He was in the team of scientists who tested graphene-based materials for applications in space using Parabolic Flights, Sounding Rockets and Lunar Rover among others.

Dr. Abusaieh, SVP for Technology & Advanced Materials at Strata Manufacturing PJSC (a Mubadala Company), oversees advanced materials portfolio, R&D strategy, and technology development. With 15 years in the US aerospace industry, he managed R&D organizations for aircraft structures, satellite hardware, and advanced materials, leading programs for NASA, AFRL, and others. Holding degrees from Villanova and Drexel University, he co-authored patents/publications and represented industry in panels/seminars. Dr. Abusaieh evaluates business opportunities in emerging technologies for Mubadala, and serves on senior management boards in academia and industry.

Yahya Zweiri (Member, IEEE) received his Ph.D. degree from King's College London. He is currently a Professor at the Department of Aerospace Engineering and Director of the Advanced Research and Innovation Center, Khalifa University of Science and Technology, UAE. His research interests include robotics with particular emphasis on applied artificial intelligence aspects and neuromorphic vision systems.